Research Square

Preprints are preliminary reports that have not undergone peer review.
They should not be considered conclusive, used to inform clinical practice,
or referenced by the media as validated information.

Receptor Activator of Nuclear Factor-κB Ligand (RANKL)-Induced DNA Damage Promotes Thyroid Cancer Bone Metastasis via Endoplasmic Reticulum Stress and Hedgehog Signaling

Weiyuan Ma
Second Hospital of Hebei Medical University
Yuxin Ma
Second Hospital of Hebei Medical University
Hanjing Cui
Second Hospital of Hebei Medical University
Yan Wei
Second Hospital of Hebei Medical University
Qiang Luo
Second Hospital of Hebei Medical University
Zengfang Hao
Second Hospital of Hebei Medical University
Jingjing He
Second Hospital of Hebei Medical University
Pengxin Zhao
28301926@hebmu.edu.cn

Second Hospital of Hebei Medical University

Research Article

Keywords: bone metastasis, receptor activator of nuclear factor-κB ligand, DNA damage, endoplasmic reticulum stress, thyroid cancer

Posted Date: August 20th, 2026

DOI: https://doi.org/10.21203/rs.3.rs-10596464/v1

License: This work is licensed under a Creative Commons Attribution 4.0 International License.
Read Full License

Additional Declarations: No competing interests reported.

Abstract

Objective

To investigate the role of RANKL in the initiation and progression of bone metastasis in thyroid cancer.

Methods

We first retrospectively analyzed clinical data to identify factors associated with bone metastasis. In vitro, we compared the expression of RANK/RANKL signaling components and downstream targets in thyroid cancer cells, and verified the effects by pharmacologic inhibition or genetic knockdown of RANKL. RANKL-overexpressing and RANKL-silenced cell lines were generated to assess DNA damage responses. Endoplasmic reticulum stress (ER stress) was induced, and the expression of ER stress-related proteins was evaluated under different RANKL levels. DNA damage signaling was then inhibited to determine its impact on ER stress. Finally, Hedgehog pathway activity was measured under varying RANKL expression and ER stress conditions.

Results

In patients, RANKL, γ-H2AX, Ki-67, and ATF6 were markedly higher in bone-metastatic than in non-metastatic thyroid tumors, and tumor tissues exhibited more pronounced DNA damage and ER stress than adjacent non-neoplastic tissues. In cell lines, RANKL overexpression accelerated proliferation, increased the S-phase population, and reduced apoptosis. RANKL knockdown had the opposite effects. Transcriptomic analysis showed that RANKL levels correlated with the expression of DNA damage, ER stress, and Hedgehog genes. Electron microscopy confirmed that RANKL suppression attenuated ER stress and Hedgehog signaling. In vivo, HDAC inhibition reduced tumor volume, and the combination of an HDAC inhibitor with RANKL knockdown further improved antitumor efficacy.

Conclusion

RANKL may promote bone metastasis of thyroid cancer by triggering DNA damage via the ER stress–Hedgehog signaling axis, and targeting this network may offer a novel therapeutic strategy.

Introduction

Bone is one of the most frequent sites of distant metastasis in patients with malignant tumors, and the management of skeletal metastases has remained a formidable clinical challenge. Over the past decade, the incidence of differentiated thyroid carcinoma (DTC) has risen markedly. Although the overall prognosis is favorable, a subset of patients present with locoregional or distant dissemination; in some cases, bone or pulmonary metastases constitute the inaugural manifestation [1, 2].

Osteoclasts are pivotal effector cells in the pathogenesis of malignant skeletal metastasis. Under pathological conditions, they are implicated in a spectrum of neoplasms, including giant-cell tumors of bone, osteosarcoma, and osseous metastases arising from thyroid carcinoma, where they facilitate local tumor invasion and progression [3, 4]. Given their active participation in both primary bone tumors and secondary bone lesions, osteoclast-targeted therapies may attenuate tumor dissemination and local extension, thereby reducing the incidence of distant metastases and associated mortality [5]. Accumulating evidence has revealed that metastatic tumor cells acquire bone marrow-associated phenotypic traits and molecular markers that confer motility, marginalization, migratory capacity, chemotactic responsiveness, phagocytic activity, angiogenic potential, matrix-degrading ability, and resistance to cytotoxic chemotherapy [6, 7].

Microenvironmental remodeling generates a “fertile soil” that is indispensable for skeletal colonization by disseminated tumor cells. Upon establishment of bone metastasis, cancer stem-like cells that have spontaneously detached from the primary lesion execute a highly coordinated cascade — local invasion, intravasation, survival in the circulation, extravasation, and ultimately homing to and engraftment within the bone parenchyma. Within this specialized niche, the engrafted cells elaborate a spectrum of cytokines, growth factors, and exosomes that further reprogram the microenvironment.

Osteoclastogenesis is predominantly governed by the receptor activator of nuclear factor-κB (RANK)/RANK ligand (RANKL) axis. Both RANK and RANKL are frequently expressed by neoplastic and stromal constituents of the tumor microenvironment [8, 9]. Aberrant activation of the RANKL/RANK pathway has been documented in thyroid, breast, prostate, endometrial, cervical, gastric, esophageal, and bladder malignancies, and its overexpression portends an unfavorable prognosis [10, 11]. RANKL stimulation elicits DNA damage and p16/p19-mediated cellular senescence; this genotoxic stress paradoxically sustains the stem-cell properties of RANK/RANKL-driven tumor cells [12]. Although the initial response may transiently restrain tumor proliferation, the senescence-associated secretory phenotype ultimately fuels tumor progression and metastatic dissemination.

DNA damage-inducible transcript 3 (DDIT3/CHOP) additionally modulates adipogenic and osteogenic lineage allocation in vitro and in vivo and fine-tunes osteoclast differentiation and function [13, 14]. Emerging evidence further suggests that DNA damage responses intersect with Hedgehog signaling and endoplasmic reticulum stress (ER stress) pathways to coordinate bone homeostasis.

Materials and Methods

All procedures were approved by the Institutional Review Board of our Hospital (IRB-2023) and conducted in accordance with the Declaration of Helsinki. Written informed consent was obtained from every participant prior to enrollment.

1. Study Design and Participants

Cohort Definition. This single-center, cross-sectional study recruited three well-defined cohorts between January 2022 and December 2023: Group A (n = 50): consecutive, treatment-naïve patients with newly diagnosed differentiated thyroid carcinoma (DTC) and synchronous bone metastases confirmed by ^{18}F-FDG PET/CT and/or histology. Group B (n = 50): consecutive, treatment-naïve patients with newly diagnosed DTC but without radiologic or histologic evidence of bone involvement. Group C (n = 20): age- (± 3 years) and sex-matched healthy volunteers undergoing routine physical examinations at our hospital's Preventive Medicine Center. Exclusion criteria for all groups were prior malignancy, systemic inflammatory disease, recent (< 3 months) surgery, or glucocorticoid/bisphosphonate use.

Sample Collection and Processing.

Peripheral Blood. After an overnight fast, 10 mL venous blood was drawn into EDTA-K_2 tubes (BD Vacutainer, USA). Plasma: samples were centrifuged at 1,500 × g for 15 min at 4°C; aliquots were snap-frozen in liquid nitrogen and stored at − 80°C. PBMCs: isolated by density-gradient centrifugation on Ficoll-Paque™ PLUS (GE Healthcare, USA), washed twice in ice-cold PBS (pH 7.4), lysed in TRIzol™ Reagent (Invitrogen, USA), and stored at − 80°C until RNA extraction.

Tissue Specimens. From Group A patients undergoing curative-intent surgery, representative tumor tissues and matched adjacent non-neoplastic thyroid parenchyma (≥ 2 cm from the macroscopic margin) were procured. Tissues were fixed in 10% neutral-buffered formalin for 24 h, routinely processed, and embedded in paraffin. Serial 4-μm sections were cut for immunohistochemistry (IHC).

Immunohistochemistry. Sections were deparaffinized in xylene, rehydrated through graded ethanol, and subjected to heat-induced antigen retrieval in citrate buffer (pH 6.0) using a pressure cooker (95°C, 20 min). Endogenous peroxidase was quenched with 3% H_2O_2 for 10 min. After blocking with 5% BSA for 30 min, sections were incubated overnight at 4°C with the following primary antibodies: RANKL (clone EPR21801, ab45039, 1:200; Abcam, USA); γ-H2AX (clone EP854(2)Y, ab229914, 1:400; Abcam, USA); Ki-67 (clone SP6, ab16667, 1:300; Abcam, USA); ATF6 (clone EPR21796, ab263955, 1:250; Abcam, USA). Detection was carried out with the EnVision™+ HRP system (Dako, Denmark) using 3,3'-diaminobenzidine (DAB) as chromogen. Sections were counterstained with Mayer's hematoxylin, dehydrated, cleared, and mounted. Negative controls were prepared by omitting the primary antibody; positive controls were tonsillar tissue for RANKL and Ki-67, and γ-irradiated fibroblasts for γ-H2AX.

2. Isolation and Cryopreservation of Peripheral Blood Mononuclear Cells (PBMCs)

Residual whole-blood samples remaining after routine laboratory testing were obtained from newly diagnosed DTC patients and age-matched healthy controls following approval by the local Ethics Committee (IRB-2023) and written informed consent.

PBMC Isolation. Blood was collected in sodium-heparin Vacutainers (R22390, Yuanye, China) and processed within 2 h. Plasma removal: after centrifugation at 400 × g for 10 min at room temperature (RT), the upper plasma layer was aspirated and stored at − 80°C. Density-gradient separation: the cell pellet was resuspended in an equal volume of sterile phosphate-buffered saline (PBS, pH 7.4) and gently layered onto an equal volume of lymphocyte separation medium (Ficoll-Paque™ PLUS, SCR005, Roche, USA). Samples were centrifuged at 800 × g for 20 min (RT, brake off). PBMC harvest: the mononuclear cell ring was collected, washed twice with PBS (400 × g, 8 min), and treated with erythrocyte lysis buffer (11814389001, Roche, USA) for 5 min at RT to remove residual red blood cells. Wash and count: cells were washed again in PBS, resuspended in complete RPMI-1640 (10% FBS, 1% penicillin–streptomycin), and counted using a Countess II automated cell counter (Thermo Fisher Scientific, USA).

Sample Allocation and Cryopreservation. Fresh PBMCs were split into two aliquots: Flow cytometry: 1 × 10^6 cells per sample were immediately stained for immunophenotyping. Molecular analyses: 2 × 10^6 cells per sample were pelleted, snap-frozen in liquid nitrogen, and stored at − 80°C for subsequent RNA isolation (RT-qPCR, PRISM 7500, Applied Biosystems, USA) and protein extraction (BCA assay, CS1125, Thermo Scientific, USA).

3. Cell Proliferation Assay (MTT)

Cell Seeding. Log-phase cells from each experimental group were detached with 0.25% trypsin–EDTA, counted, and seeded into 96-well plates at 5 × 10^3 cells per well in 100 µL complete medium. Each condition was run in quadruplicate. Plates were incubated at 37°C with 5% CO_2 in a humidified incubator (Forma™ Series II, model 55836, Thermo Scientific, USA).

MTT Protocol. At 24, 48, and 72 h post-seeding, 50 µL of MTT reagent (5 mg/mL in PBS, M5655, Merck, USA) was added to each well. After 4 h incubation at 37°C, the supernatant was carefully aspirated and replaced with 150 µL dimethyl sulfoxide (DMSO, Sigma-Aldrich, USA) to dissolve formazan crystals. Plates were gently agitated for 10 min at room temperature in the dark, and absorbance was measured at 490 nm using a Varioskan LUX multimode microplate reader (Thermo Fisher Scientific, USA). Background-corrected data were normalized to the 0 h baseline and expressed as fold change relative to the control.

4. Western Blot Analysis of Endoplasmic Reticulum Stress (ER Stress) and Hedgehog Signaling Pathway Proteins

4. Western Blot Analysis of Endoplasmic Reticulum Stress (ER Stress) and Hedgehog Signaling Pathway Proteins

Protein Extraction and Quantification. Cells were lysed on ice for 30 min in RIPA buffer (P0013B, Beyotime, China) supplemented with 1 mM phenylmethylsulfonyl fluoride (PMSF) and a 1% protease/phosphatase inhibitor cocktail (P1046, Beyotime). Lysates were cleared by centrifugation at

12,000 × g for 15 min at 4°C. Protein concentrations were determined with a BCA assay kit (CS1125, Thermo Scientific, USA) according to the manufacturer's instructions.

Electrophoresis and Immunoblotting. Equal amounts of protein (30 μg) were resolved on 10% SDS-PAGE gels and transferred to 0.22-μm PVDF membranes (IPVH00010, Millipore). After blocking with 5% non-fat milk in Tris-buffered saline containing 0.1% Tween-20 (TBST) for 1 h at room temperature, membranes were incubated overnight at 4°C with the following primary antibodies (all from Abcam unless specified): GAPDH (loading control; ab8245, mouse mAb [6C5], 1:10,000); ATF6 (ab122897, rabbit polyclonal, 1:1,000); RIPK1 (ab300617, rabbit mAb [EPR24883-85], 1:1,000); PERK (ab229912, rabbit mAb [EPR19876-294], 1:1,000); GLI1 (ab134906, rabbit mAb [EPR4523], 1:1,000); SHH (ab308225, rabbit mAb [HL2076], 1:1,000); Smoothened (ab236465, rabbit polyclonal, 1:1,000). Membranes were washed three times with TBST and incubated for 1 h at room temperature with HRP-conjugated secondary antibodies: goat anti-mouse IgG (C31430100, 1:10,000; Thermo Fisher, USA) or goat anti-rabbit IgG (C31460100, 1:10,000; Thermo Fisher, USA). Immunoreactive bands were visualized using an enhanced chemiluminescence substrate (ECL-PLUS, GE Healthcare) and captured with the ImageQuant LAS 4010 imaging system (GE Healthcare, USA). Band intensities were quantified by densitometry using ImageJ (NIH, USA) and normalized to GAPDH.

Pharmacological Modulation of Hedgehog Signaling. To confirm pathway specificity, cells were treated for 24 h with the Smoothened agonist SAG analogue (trans-isomer; sc-396539, Santa Cruz, USA) at 200 nM or vehicle control (0.1% DMSO). Protein expression changes were subsequently analyzed as described above.

5. Transmission Electron Microscopy (TEM) Analysis of Cellular Ultrastructure

Sample Preparation. The culture medium was aspirated, and cells were gently rinsed twice with pre-warmed PBS (pH 7.4). Fixation was initiated by adding 2.5% (v/v) electron-microscopy (EM)-grade glutaraldehyde in 0.1 M sodium cacodylate buffer (pH 7.2) at room temperature (RT) for 5 min in the dark. The monolayer was detached with a single, unidirectional sweep of a sterile cell scraper to minimize mechanical trauma; repetitive scraping was strictly avoided. The cell suspension was transferred into a 1.5 mL microcentrifuge tube and pelleted at 500 × g for 2 min at 4°C. After discarding the supernatant, the pellet (≈ 1 mm^3) was re-fixed in fresh 2.5% glutaraldehyde overnight at 4°C.

Post-Fixation and Embedding. Following three washes with 0.1 M cacodylate buffer, specimens were post-fixed in 1% osmium tetroxide (OsO_4) for 1 h at 4°C, dehydrated through a graded ethanol series (30%, 50%, 70%, 90%, 100% × 3), and infiltrated with Epon 812 resin using a standard protocol. Ultrathin sections (70 nm) were cut on a Leica UC7 ultramicrotome (Leica Microsystems, Germany), mounted on 200-mesh copper grids, and stained with 2% uranyl acetate (15 min) and 0.5% lead citrate (5 min).

Image Acquisition. Specimens were imaged with a Talos F200X transmission electron microscope (Thermo Fisher Scientific, USA) operated at 200 kV. Representative micrographs (×8,000 to ×80,000) were captured using a Ceta 16M CMOS camera. Membrane integrity and intracellular membrane systems were evaluated by two independent investigators blinded to experimental conditions.

6. Single-Cell Gel Electrophoresis (Comet) Assay

Slide Preparation. Log-phase cells were harvested by gentle trypsinization, washed twice with ice-cold PBS, and resuspended at 1 × 10^5 cells/mL. A 1% (w/v) solution of low-melting-point agarose (LMA; SeaPlaque™ GTG™, Lonza, USA) was prepared in PBS, equilibrated to 37°C, and mixed 1:10 (v/v) with the cell suspension to obtain a final agarose concentration of 0.75%. Eighty microliters of the cell–agarose mixture were immediately pipetted onto CometSlide™ 20-well slides (Trevigen, USA) pre-coated with 0.5% normal-melting-point agarose and allowed to gel for 10 min at 4°C in the dark.

Lysis and Alkaline Unwinding. Gels were immersed in pre-chilled lysis buffer (2.5 M NaCl, 100 mM EDTA, 10 mM Tris, 1% Triton X-100, 10% DMSO, pH 10) for 1 h at 4°C to remove cellular proteins. Slides were then transferred to an alkaline unwinding solution (300 mM NaOH, 1 mM EDTA, pH > 13) for 30 min at 4°C in the dark to facilitate DNA denaturation. Slides were placed in a horizontal electrophoresis tank (CometAssay® ES unit, Trevigen) containing alkaline electrophoresis buffer (300 mM NaOH, 1 mM EDTA, pH > 13) maintained at 4°C. Electrophoresis was conducted for 20 min at 25 V (≈ 0.74 V/cm) and 300 mA. After electrophoresis, slides were neutralized twice (5 min each) in 0.4 M Tris-HCl (pH 7.5), dehydrated in 70% (v/v) ethanol for 5 min, and air-dried at RT.

Staining and Imaging. Dried gels were stained with SYBR™ Gold nucleic acid stain (1:10,000 in TE buffer; Invitrogen, USA) for 20 min at 4°C in the dark. Slides were examined under a fluorescence microscope (Axio Observer 7, Zeiss, Germany) using a 20× objective (excitation 490 nm; emission 520 nm). Fifty randomly selected comets per sample were analyzed with Comet Assay IV software (Perceptive Instruments, UK). DNA damage was quantified as the percentage of DNA in the tail (% tail DNA; tail intensity/total intensity × 100). All experiments were performed in triplicate and conducted under dim light to prevent photo-induced DNA damage.

7. Immunofluorescence Staining and Confocal Microscopy

Slide Preparation. Cells were harvested, washed twice with ice-cold PBS, and adjusted to 1 × 10^5 cells/mL. Two hundred microliters of the suspension were evenly dispensed onto poly-L-lysine-coated glass slides (Thermo Scientific, USA) and allowed to settle for 30 min at 37°C in a humidified chamber.

Fixation and Permeabilization. Slides were fixed sequentially: 100% methanol, − 20°C, 10 min; 2% (w/v) paraformaldehyde in PBS, RT, 15 min. After three PBS washes (5 min each), cells were permeabilized with 0.2% Triton X-100 in PBS for 5 min on ice, followed by three additional PBS washes. Non-specific binding was blocked with 5% (w/v) non-fat dry milk in PBS for 60 min at RT. Primary antibodies were

diluted in antibody diluent (PBS containing 1% BSA and 0.05% Tween-20) and applied overnight at 4°C in a humidified chamber. Slides were washed three times (5 min each) with PBS-T (0.05% Tween-20). Corresponding Alexa Fluor-conjugated secondary antibodies (Invitrogen, USA; 1:1,000) were incubated for 1 h at RT in the dark. Following three PBS-T washes, nuclei were counterstained with DAPI (1 μg/mL), and the slides were mounted using Fluoromount-G™ (SouthernBiotech, USA).

Imaging and Storage. Fluorescence images were acquired using a Zeiss LSM 980 confocal microscope (Zeiss, Germany) equipped with 405 nm, 488 nm, and 561 nm laser lines. Optical sections (0.5 μm z-step) were collected with a 63× oil-immersion objective (NA 1.4) and processed with Zen Black 3.2 software. All images were captured under identical acquisition settings for each channel. Stained slides were stored at 4°C in the dark and imaged within 48 h to minimize fluorophore degradation.

8. NOD/SCID Subcutaneous Xenograft Model

Animals. Female NOD.CB17-Prkdc^{scid}/NcrCrl (NOD/SCID) mice aged 5–6 weeks (14–18 g) were purchased from Charles River Laboratories (Beijing, China). All procedures were approved by the Institutional Animal Care and Use Committee (IACUC-2023) and conducted in accordance with the ARRIVE 2.0 and NIH guidelines. Mice were housed under specific-pathogen-free (SPF) conditions (20–24°C, 45–65% humidity, 12 h light/12 h dark cycle) with ad libitum access to irradiated food and autoclaved water.

Irradiation and Cell Inoculation. Mice received a single sublethal dose of 220 cGy total-body irradiation (X-RAD 320, Precision X-Ray, USA) 4 h prior to cell injection. Log-phase human thyroid cancer cells (1×10^6 cells/100 μL Matrigel®:PBS = 1:1) were implanted subcutaneously into the right dorsal flank using a 25 G needle. Each experimental group comprised n = 5 mice.

Tumor Monitoring and Randomization. Tumor dimensions were measured three times weekly with digital Vernier calipers. Tumor volume (V) was calculated as $V = 0.5 \times a \times b^2$, where a and b are the longest and perpendicular diameters, respectively. When the mean tumor volume reached approximately 50 mm³ (Day 7–10 post-inoculation), mice were randomly assigned (simple randomization by computer-generated sequence) to one of four treatment groups: scramble control, RANKL knockdown (shRANKL), vorinostat treatment, or combined RANKL knockdown and vorinostat treatment. Vorinostat was administered intraperitoneally at 50 mg/kg once daily; RANKL knockdown was achieved by stable lentiviral shRNA transduction of the implanted cells prior to inoculation.

Endpoint and Tissue Collection. Animals were monitored daily; humane endpoints were applied when tumor volume exceeded 1,500 mm³, ulceration developed, or body-weight loss exceeded 15%. At study termination, mice were euthanized by CO_2 asphyxiation followed by cervical dislocation. Tumors were excised, weighed, measured, and bisected: one half was snap-frozen in liquid nitrogen for molecular analyses, and the other half was fixed in 10% neutral-buffered formalin for 24 h, paraffin-embedded, and sectioned at 4 μm for subsequent histological and immunohistochemical studies.

9. Statistical Analysis

All statistical analyses were performed using IBM SPSS Statistics 28.0 (IBM Corp., USA) and GraphPad Prism 9.5 (GraphPad Software, USA). Data distribution was assessed with the Shapiro–Wilk test and visual inspection of Q–Q plots. Continuous variables are presented as mean ± standard deviation (SD) for normally distributed data or median (interquartile range, IQR) for non-normally distributed data. Comparisons between two independent groups were performed using two-tailed unpaired Student's *t*-tests (parametric) or Mann–Whitney *U* tests (non-parametric), as appropriate. For multiple-group comparisons, one-way analysis of variance (ANOVA) followed by Tukey's post hoc test, or the Kruskal–Wallis test followed by Dunn's multiple-comparison test, was employed. Pearson's correlation coefficient (r) was calculated to evaluate linear associations between normally distributed continuous variables; otherwise, Spearman's rank correlation was used. Unless otherwise stated, all in vitro experiments were performed in at least three independent biological replicates. All tests were two-sided, and a P value < 0.05 was considered statistically significant.

Results

1. Upregulation of osteoclastogenic, proliferative, DNA damage, and endoplasmic reticulum (ER) stress pathways in thyroid cancer with bone metastasis

Clinical characteristics. Baseline demographics and clinicopathological variables were comparable between patients with thyroid cancer (TC) with synchronous bone metastasis (BM) and those without BM (Supplementary Table 1). Detailed anatomical sites of skeletal involvement are provided in Supplementary Table 2.

Immunohistochemistry. Paraffin-embedded specimens were stained for key signaling molecules. Quantitative immunoreactivity scores (IRS, range 0–12) revealed significantly higher expression of RANKL (mediator of osteoclastogenesis), Ki-67 (proliferation), γ-H2AX (DNA damage marker), and ATF6 (ER stress sensor) in BM-positive tumors than in BM-negative tumors (all $P < 0.001$). All four proteins were likewise markedly upregulated in TC tissues relative to matched adjacent non-neoplastic thyroid parenchyma (Fig. 1A).

Transcriptional profiling. RT-qPCR analyses corroborated the immunohistochemical findings. Transcript levels of *ATR*, *ATM*, *H2AFX*, *CHEK1*, and *CHEK2* were elevated in BM-positive tumors compared with BM-negative tumors (Fig. 1B). Notably, *ATR*, *ATM*, and *H2AFX* mRNA exhibited the greatest differential expression (fold change > 2.5, $P < 0.01$). Across the entire cohort, each DNA damage indicator was significantly higher in malignant tissue than in adjacent non-neoplastic tissue.

ER stress axis activation. Similarly, expression of canonical ER stress mediators — *ATF6*, *RIPK1*, *EIF2AK3* (PERK), and *EIF2S1* — was significantly increased in BM-positive tumors than in BM-negative tumors ($P < 0.001$; Fig. 1C). Again, malignant tissue displayed markedly higher ER stress activity than adjacent non-neoplastic tissue. Collectively, these data demonstrate that thyroid cancer with bone metastasis is

characterized by concerted activation of osteoclastogenic, proliferative, DNA damage, and ER stress signaling networks.

2. RANKL promotes thyroid carcinoma cell proliferation and survival

Basal expression profiling. Quantitative RT-PCR and Western blot analyses revealed that the non-neoplastic thyroid follicular epithelial cell line Nthy-ori 3 − 1 expressed significantly lower RANKL mRNA and protein levels than the three thyroid carcinoma cell lines tested (TPC-1, MDA-T32, and SW579) (Fig. 2A). Based on these data, TPC-1 and SW579 — lines with intermediate and high basal RANKL expression, respectively — were selected for lentiviral manipulation.

Lentiviral transduction efficiency. Cells were transduced with either shRNA targeting RANKL (shRANKL), full-length RANKL cDNA (OE-RANKL), or non-targeting/scrambled controls. Transduction efficiency exceeded 95%, as determined by GFP positivity (flow cytometry) (Fig. 2B; Supplementary Fig. 2A).

Validation of engineered expression. qRT-PCR confirmed a ≥ 50% reduction in RANKL mRNA in shRANKL cells and a ≥ 2-fold increase in OE-RANKL cells relative to scrambled controls (Figs. 2C and 2D).

Functional consequences. MTT assays performed over 72 h demonstrated that RANKL knockdown significantly attenuated growth ($P < 0.01$), whereas RANKL overexpression accelerated proliferation ($P < 0.001$) (Figs. 2E and 2F). Cell-cycle analysis (propidium iodide staining) revealed that RANKL overexpression increased the proportion of cells in S phase ($P < 0.01$), whereas RANKL depletion induced G1 arrest (Figs. 2G and 2H).

Apoptosis profiling. Western blot analysis of canonical apoptosis markers showed that RANKL silencing reduced Bcl-2 expression and increased cleaved caspase-3 and Bax levels (Fig. 2I), indicating enhanced apoptosis. Collectively, these data establish RANKL as a key driver of proliferation and survival in thyroid carcinoma cells.

3. RANKL coordinates DNA damage, endoplasmic reticulum (ER) stress, and Hedgehog signaling in thyroid carcinoma cells

Differential gene-expression analysis revealed that RANKL manipulation significantly altered the mRNA levels of key pathway components, including DNA damage response genes (*ATR*, *ATM*, *H2AFX*, *CHEK1*, *CHEK2*), ER stress mediators (*ATF6*), and Hedgehog (Hh) signaling molecules (*SMO*, *GLI1*, *SHH*).

Ultrastructural evidence of ER stress activation. Transmission electron microscopy of RANKL-overexpressing cells demonstrated pronounced ER dilation and increased vesiculation — morphological hallmarks of active ER stress (Fig. 3A; Supplementary Fig. 2B). These changes were absent in control cells and attenuated under RANKL knockdown conditions. RT-qPCR analysis confirmed the transcriptomic findings: depletion of RANKL significantly reduced the transcript levels of *ATF6* (ER

stress) and *SHH* (Hh ligand) (Fig. 3B, 3C). Conversely, forced RANKL expression elevated *ATF6*, *SMO*, *GLI1*, and *SHH* mRNA abundance (Fig. 3D, 3E). All changes were consistent across both cell lines. Western blot analyses confirmed that RANKL overexpression increased ATF6, SMO, GLI1, and SHH protein levels, whereas RANKL knockdown produced the opposite effect. Bioinformatic analysis indicated that altered RANKL expression may influence the activation of downstream signaling pathways (Supplementary Fig. 2B).

Functional impact on apoptosis. Annexin V/PI flow cytometry showed that the apoptotic fraction increased upon RANKL knockdown and decreased upon RANKL overexpression (Fig. 3G). Immunoblotting revealed that RANKL silencing increased the expression of pro-apoptotic proteins (cleaved caspase-3, Bax) and decreased anti-apoptotic Bcl-2, whereas RANKL overexpression produced the converse signature (Fig. 3F, 3H). Collectively, these data demonstrate that RANKL coordinates a transcriptional program that integrates DNA damage sensing, ER stress signaling, and Hedgehog pathway activation, thereby modulating cell survival and apoptosis in thyroid carcinoma cells.

4. RANKL promotes DNA damage accumulation in thyroid carcinoma cells

Single-cell DNA damage assessment. Alkaline comet assays revealed that deregulated RANKL expression significantly increased DNA damage. Compared with controls, RANKL-overexpressing cells exhibited markedly increased tail moment and the percentage of DNA in the tail (% tail DNA) (Fig. 4A, B), reflecting greater numbers of DNA breaks, longer migrated fragments, and elevated overall damage load. Conversely, RANKL knockdown reduced both parameters ($P < 0.001$, n = 150 comets per condition).

Transcriptional regulation of the DNA damage response. Quantitative RT-PCR demonstrated that RANKL knockdown decreased *ATM* and *H2AFX* mRNA expression (Fig. 4C), whereas forced RANKL expression increased *ATM*, *H2AFX*, *CHEK1*, and *CHEK2* transcripts (Fig. 4D). These changes were concordant across TPC-1 and SW579 cell lines. Immunoblotting confirmed that total and phosphorylated ATM (p-ATM^{Ser1981}) and γ-H2AX protein levels increased with RANKL abundance (Fig. 4E). RANKL depletion reduced both basal and etoposide-induced γ-H2AX foci, whereas RANKL overexpression amplified the response ($P < 0.01$).

Cytoskeletal correlates. Immunofluorescence confocal microscopy revealed that aberrant RANKL expression was accompanied by disorganized microfilament and microtubule networks (Fig. 4F). Immunofluorescence also revealed upregulated ER stress proteins and increased DNA damage upon RANKL overexpression (Supplementary Fig. 3B–C). These architectural defects were accompanied by activated ER stress markers (GRP78 and phospho-PERK), implicating ER stress-associated cytoskeletal instability as a potential mechanistic link between RANKL signaling and DNA damage accumulation. Together, these data establish RANKL as a critical upstream regulator that amplifies DNA damage signaling and compromises genomic integrity in thyroid carcinoma cells.

5. In vivo evaluation of the effects of RANKL knockdown on DNA damage, ER stress, and Hedgehog signaling

Female NOD/SCID mice (n = 5 per group) bearing subcutaneous TPC-1 tumors were randomized to: (i) scramble control, (ii) RANKL knockdown (shRANKL), (iii) HDAC inhibitor (vorinostat, 50 mg/kg i.p. daily), or (iv) combined shRANKL and vorinostat. Tumor volumes were monitored three times weekly. Compared with the scramble control group, shRANKL alone suppressed tumor growth by 46% ($P < 0.01$), whereas vorinostat monotherapy reduced tumor burden by 38% ($P < 0.05$). Combined treatment elicited a 72% reduction relative to the scramble control group at study endpoint ($P < 0.001$; Fig. 5A, B) without overt toxicity (body-weight loss < 5%).

Molecular profiling of excised tumors. Immunohistochemical analysis of terminal tumors revealed that RANKL knockdown significantly decreased nuclear γ-H2AX (DNA damage marker), ATF6 (ER stress sensor), and SHH (Hedgehog ligand) immunoreactivity (a reduction in IRS of > 60%, $P < 0.01$; Fig. 5C). Vorinostat further downregulated these proteins, an effect that was most pronounced in the combination arm (a reduction in IRS of > 80%, $P < 0.001$).

Therapeutic implications. These data indicate that RANKL inhibition cooperates with HDAC inhibition to attenuate DNA damage/ER stress/Hedgehog signaling in vivo, providing a rational basis for combined epigenetic and RANKL-targeted therapy in aggressive thyroid cancer.

Discussion

The RANKL/RANK axis is emerging as a pleiotropic regulator that may converge on DNA damage signaling, ER stress, and Hedgehog pathway activation to influence thyroid-cancer bone metastasis. Our findings provide a mechanistic framework that integrates these previously disparate lines of evidence.

RANKL/RANK as a candidate onco-immunological hub. RANKL-mediated osteoclastogenesis is canonically governed by the RANKL/RANK/OPG triad. In neoplastic contexts, however, the same ligand–receptor pair has been reported to drive a broader immunomodulatory program. Tumor-infiltrating Treg cells secrete RANKL and upregulate RANK on tumor-associated macrophages (TAMs), generating a self-reinforcing immunosuppressive loop that may foster tumor growth, angiogenesis, and metastasis [7]. RANKL also enhances dendritic-cell survival and polarizes CD4 + T cells toward a TH1 phenotype; yet within the tumor microenvironment, this pro-inflammatory effect may be overridden by compensatory checkpoints. Because the present study employed immunodeficient NOD/SCID hosts, our data do not directly address these immune-dependent mechanisms, which remain to be tested in immunocompetent models. Pre-clinical studies show that RANKL blockade may synergize with anti-CTLA-4 antibodies, underscoring the therapeutic potential of combining RANKL inhibition with immune-checkpoint blockade [8, 26].

RANKL-associated DNA damage response and genomic instability. Beyond its immunological functions, RANKL has been linked to activation of an ATM–CHK2–p53-mediated DNA damage response (DDR).

Germline defects in DDR genes are well-established drivers of heritable thyroid and breast carcinomas, and we now show that RANKL overexpression is associated with elevated ATM, γ-H2AX, CHK1, and CHK2. These alterations may culminate in replication stress, premature senescence, and acquisition of stem-like properties — events that could accelerate metastatic dissemination [11, 12]. Conversely, RANKL knockdown restored genomic integrity, as evidenced by reduced tail moment in comet assays.

DDIT3 as a potential mediator coupling ER stress to osteoclast biology. DNA damage-inducible transcript 3 (DDIT3/CHOP) integrates stress sensing with lineage-fate decisions. In bone marrow macrophages, DDIT3 restrains RANKL-induced osteoclast formation via the C/EBPα–CTSK axis and blunts MAPK–Akt activation. Our data are consistent with the possibility that, in thyroid-cancer cells, RANKL-induced ER stress may upregulate DDIT3, thereby modulating tumor-cell survival and osteoclastic crosstalk [14, 25]; however, DDIT3 was not directly interrogated in the present study and this proposed link remains to be experimentally confirmed.

Hedgehog signaling as a downstream effector of RANKL-mediated ER stress. Hedgehog ligands (SHH, IHH, DHH) and their downstream effector GLI1 are amplified under ER stress conditions [21]. Our transcriptomic and ultrastructural analyses are consistent with RANKL overexpression promoting ER stress and increased GLI1 expression, potentially through the PERK–eIF2α–ATF4 axis [22]; nonetheless, only PERK was assessed at the protein level in the present study, and phosphorylation of PERK, eIF2α, and ATF4 induction were not directly measured. These proposed events converge on increased GLI1 expression and transcriptional activation of pro-proliferative and pro-invasive genes [17–20]. Because pharmacological or genetic attenuation of Hedgehog signaling (e.g., SANT-1, GANT61) was not performed in this study, the hierarchical relationship between RANKL and the Hedgehog pathway remains to be formally established.

Translational implications of HDAC inhibition. Histone deacetylases (HDACs) compact chromatin and repress DDR and ER stress genes. HDAC inhibitors (HDACi) hyperacetylate histones, restore chromatin accessibility, and may synergize with RANKL knockdown to suppress tumor growth in vivo. Our xenograft studies showed that combined RANKL knockdown and vorinostat reduced tumor volume by 72%, accompanied by downregulation of γ-H2AX, ATF6, and SHH. These findings provide a mechanistic rationale for combining epigenetic and RANKL-targeted therapies in patients with bone-metastatic thyroid cancer [26, 27].

Limitations and future directions. Several limitations should be acknowledged. First, the human component was a single-center, cross-sectional analysis with modest group sizes, limiting causal inference and generalizability. Second, in vivo efficacy was evaluated in a subcutaneous xenograft model using immunodeficient mice, which does not recapitulate the bone microenvironment of skeletal metastasis nor the intact immune contribution to the RANKL/RANK axis. Third, several proposed mechanistic links — including the PERK–eIF2α–ATF4 axis, DDIT3 induction, GLI1 nuclear translocation, and the epistatic ordering of RANKL and Hedgehog signaling — were not directly tested and are presented as hypotheses. Fourth, the in vivo sample size (n = 5 per group) was small. Future work should

incorporate orthotopic or intraosseous models, patient-derived organoids, syngeneic immunocompetent models, and prospective clinical studies to validate the efficacy and safety of RANKL/HDACi combination therapy.

Conclusions

We propose a unifying model in which RANKL overexpression in thyroid cancer may initiate a cascade of DNA damage accumulation, ER stress activation, and Hedgehog pathway amplification, thereby potentially facilitating bone metastasis. Targeting RANKL alone or in combination with HDAC inhibitors may represent a promising therapeutic strategy to disrupt this cascade and improve clinical outcomes.

Declarations

Acknowledgments

Funding and Support: This work was supported by the Research Project of the Department of Finance of Hebei Province, China (Grant No. ZF2025112).

Competing interests: The authors declare that they have no competing interests.

Author contributions: All authors participated in study design, data acquisition, and interpretation; drafted or critically revised the manuscript; and approved the final version for submission.

References

1. Varadarajan VV, Pace EK, Patel V, et al. Follicular thyroid carcinoma metastasis to the facial skeleton: a systematic review. BMC Cancer. 2017;17(1):225. doi:10.1186/s12885-017-3198-9
2. Yaşar M, Aydemir E, Ateş C, et al. Retrospective evaluation of bone metastases in patients with thyroid malignancy: a single-center experience. Cureus. 2024;16(1):e52079. doi:10.7759/cureus.52079
3. Ozger O, Kaplan N. Follicular variant of papillary thyroid carcinoma presenting with thoracic vertebral metastasis: a rare phenomenon. J Coll Physicians Surg Pak. 2022;32(3):395-397. doi:10.29271/jcpsp.2022.03.395
4. Pal P, Singh B, Kane S, et al. Bone metastases in follicular carcinoma of thyroid. Indian J Otolaryngol Head Neck Surg. 2018;70(1):10-14. doi:10.1007/s12070-017-1133-5
5. Aziz A, Masood MQ, Sattar S, et al. Follicular thyroid carcinoma in a developing country: a 10-year retrospective study. Cureus. 2021;13(7):e16594. doi:10.7759/cureus.16594
6. Jannin A, Lamartina L, Moutarde C, et al. Bone metastases from differentiated thyroid carcinoma: heterogeneous tumor response to radioactive iodine therapy and overall survival. Eur J Nucl Med Mol Imaging. 2022;49(4):1234-1244. doi:10.1007/s00259-021-05607-4

7. Delitala AP, Scuteri A, Doria C. Thyroid hormone diseases and osteoporosis. J Clin Med. 2020;9(4):1034. doi:10.3390/jcm9041034
8. Van Dam PA, Verhoeven Y, Trinh XB, et al. RANK/RANKL signaling inhibition may improve the effectiveness of checkpoint blockade in cancer treatment. Crit Rev Oncol Hematol. 2019;133:85-91. doi:10.1016/j.critrevonc.2018.11.008
9. Deligiorgi MV, Mahaira H, Eftychiadis C, et al. RANKL, OPG, TRAIL, KRas, and c-Fos expression in relation to central lymph node metastases in papillary thyroid carcinoma. J BUON. 2018;23(4):1029-1040. PMID: 30358209
10. Shin HS, Sun HJ, Whang YM, et al. Metformin reduces thyroid cancer tumor growth in the metastatic niche of bone by inhibiting osteoblastic RANKL production. Thyroid. 2021;31(5):760-771. doi:10.1089/thy.2020.0614
11. Zhou D, Yang D. MicroRNA involvement in the pathogenesis of multiple diseases by targeting osteoprotegerin. Sichuan Da Xue Xue Bao Yi Xue Ban. 2024;55(3):777-782. PMID: 38948285
12. Stolarova L, Kleiblova P, Janatova M, et al. CHEK2 germline variants in cancer predisposition: stalemate rather than checkmate. Cells. 2020;9(12):2675. doi:10.3390/cells9122675
13. Yang B, Sun H, Jia M, et al. DNA damage-inducible transcript 3 restrains osteoclast differentiation and function. Bone. 2021;153:116162. doi:10.1016/j.bone.2021.116162
14. Zhang L, Cheng X, Xu S, et al. Curcumin induces endoplasmic reticulum stress-associated apoptosis in human papillary thyroid carcinoma BCPAP cells via disruption of intracellular calcium homeostasis. Medicine (Baltimore). 2018;97(24):e11095. doi:10.1097/MD.0000000000011095
15. Rahman S, Archana A, Jan AT, et al. Molecular insights into the relationship between autoimmune thyroid diseases and breast cancer: a critical perspective on autoimmunity and ER stress. Front Immunol. 2019;10:344. doi:10.3389/fimmu.2019.00344
16. Kure S, Chiba T, Ebina A, et al. Correlation between low expression of protein disulfide isomerase A3 and lymph node metastasis in papillary thyroid carcinoma and poor prognosis: a clinicopathological study of 1,139 cases with long-term follow-up. Endocr J. 2021;68(11):1317-1327. doi:10.1507/endocrj.EJ21-0275
17. Dufresne SS, Desgeorges MM, Di Fulvio S, et al. Extra-osseous roles of the RANK-RANKL-OPG axis with a focus on skeletal muscle. Cells. 2024;13(19):1549. doi:10.3390/cells13191549
18. Bagheri-Yarmand R, Sinha KM, Li L, et al. Combinations of tyrosine kinase inhibitor and ERAD inhibitor promote oxidative stress-induced apoptosis through ATF4 and KLF9 in medullary thyroid cancer. Mol Cancer Res. 2019;17(3):751-760. doi:10.1158/1541-7786.MCR-18-0580
19. Lee YS, Lee DH, Choudry HA, et al. Ferroptosis-induced endoplasmic reticulum stress: cross-talk between ferroptosis and apoptosis. Mol Cancer Res. 2018;16(7):1073-1076. doi:10.1158/1541-7786.MCR-17-0669
20. Kato S, Demura S, Shinmura K, et al. Current management of bone metastases from differentiated thyroid cancer. Cancers (Basel). 2021;13(17):4440. doi:10.3390/cancers13174440

21. Xu X, Lu Y, Li Y, et al. Sonic Hedgehog signaling in thyroid cancer. Front Endocrinol (Lausanne). 2017;8:284. doi:10.3389/fendo.2017.00284
22. Coker-Gurkan A, Can E, Sahin S, et al. Atiprimod triggered apoptotic cell death via acting on PERK/eIF2α/ATF4/CHOP and STAT3/NF-κB axis in MDA-MB-231 and MDA-MB-468 breast cancer cells. Mol Biol Rep. 2021;48(6):5233-5247. doi:10.1007/s11033-021-06470-0
23. Tsukasaki M, Hamada K, Okamoto K, et al. RANK–RANKL–OPG axis in MASLD: current evidence linking bone and liver diseases and future perspectives. Int J Mol Sci. 2024;25(17):9193. doi:10.3390/ijms25179193
24. Zhan Y, Guo Y, Liang C, et al. RANK promotes colorectal cancer migration and invasion by activating the Ca^{2+}-calcineurin/NFATC1-ACP5 axis. Cell Death Dis. 2021;12:602. doi:10.1038/s41419-021-03642-7
25. Casimiro S, Costa L. The roadmap of the RANKL/RANK pathway in cancer. Int J Mol Sci. 2022;23(13):7155. doi:10.3390/ijms23137155
26. Peters S, Casimiro S, Costa L. RANKL/RANK pathway: beyond bone remodeling. Target Oncol. 2019;14:641-651. doi:10.1007/s11523-019-00670-1
27. Chiossone L, Chaix J, Fuseri N, et al. The RANKL-RANK axis: a bone to thymus round trip. Front Immunol. 2019;10:629. doi:10.3389/fimmu.2019.00629

Figures

Figure 1A

	N	Thyroid carcinoma (Bone metastasis)					Paracancer tissue					Thyroid carcinoma (without Bone metastasis)				
		-	+	++	+++	(%)	-	+	++	+++	(%)	-	+	++	+++	(%)
RANKL	50	8	8	23	11	84%	32	6	5	7	36%	24	5	10	11	52%
γ-H2AX	50	15	12	19	4	70%	37	4	6	3	26%	22	10	9	9	56%
Ki67	50	10	17	18	15	80%	41	3	4	2	18%	16	11	16	8	68%
ATF6	50	9	11	13	17	82%	29	9	7	5	42%	19	9	17	5	62%

Figure 1B

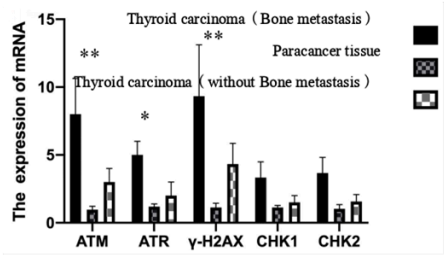


Figure 1C

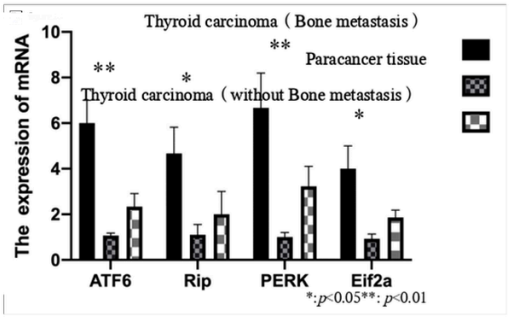


Figure 1D

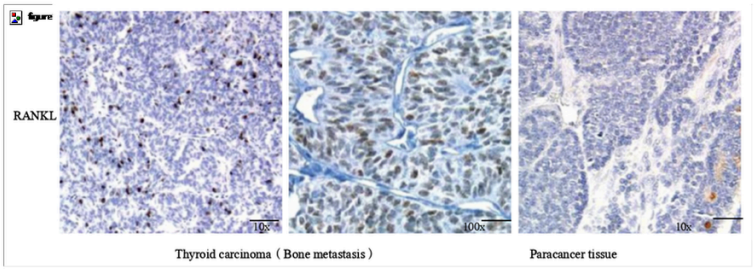


Figure 1

Osteoclastogenic, proliferative, DNA damage, and ER stress markers are upregulated in thyroid cancer with bone metastasis. (A) Quantitative immunoreactivity scores revealed significantly higher expression of RANKL, Ki-67, γ-H2AX, and ATF6 in bone-metastatic tumors. (B–C) RT-qPCR analyses corroborated the immunohistochemical findings for DNA damage and ER stress markers. (D) Immunohistochemistry confirmed differential RANKL expression among the groups.

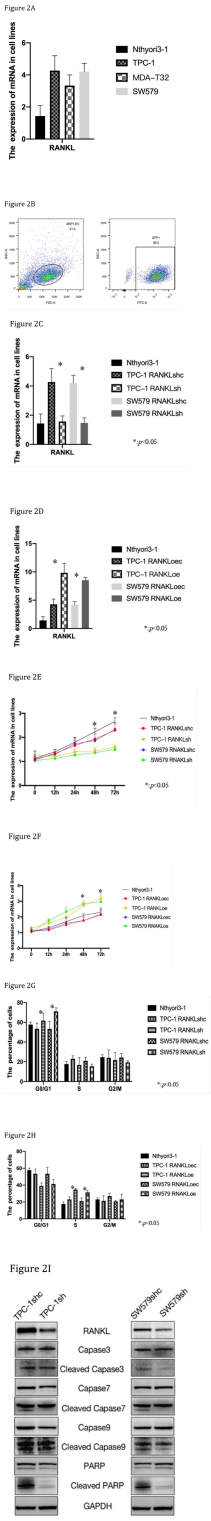


Figure 2

RANKL promotes thyroid carcinoma cell proliferation and survival. (A) Quantitative RT-PCR was used to determine RANKL expression levels across distinct cell lines. (B–D) Cell lines with differential RANKL expression levels were established. (E–F) Proliferative activity differed significantly among cell lines stratified by RANKL expression. (G–H) Cell-cycle profiles differed among cell lines stratified by RANKL

expression. (I) Western blotting revealed differential expression of apoptotic proteins in cell lines with varying RANKL levels.

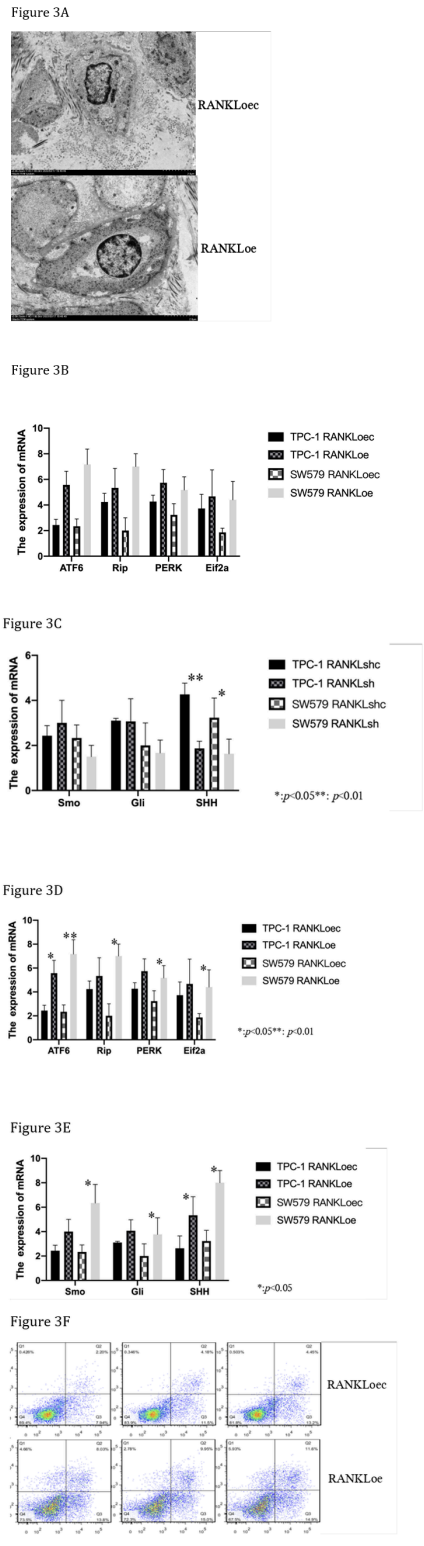


Figure 3

RANKL coordinates ER stress and Hedgehog signaling in thyroid carcinoma cells. (A) Electron microscopy revealed the impact of differential RANKL expression on ER stress in the cell lines. (B–E)

Effects of differential RANKL expression on ER stress and Hedgehog factors in cell lines. (F–H) Impact of differential RANKL expression on apoptosis in cell lines.

Figure 4A

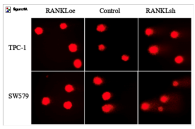


Figure 4B

	RANKLsh	Control	RANKLoe
TPC-1	4.08±1.68	6.74±1.93	9.04±1.57
SW579	6.57±1.25	11.59±2.14	19.23±3.23

Figure 4C

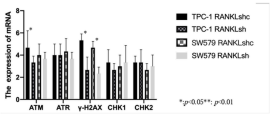


Figure 4D

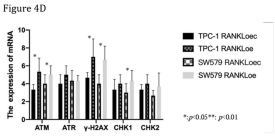


Figure 4E

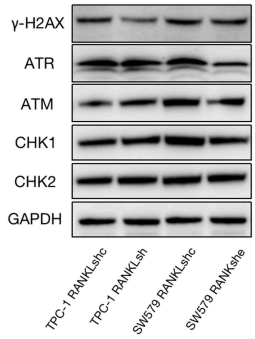


Figure 4F

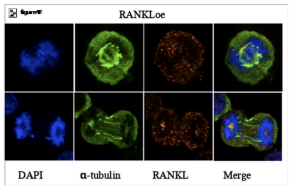


Figure 4G

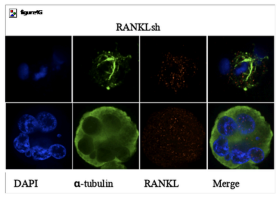


Figure 4

RANKL promotes DNA damage accumulation in thyroid carcinoma cells. (A–B) Comet assays revealed that deregulated RANKL expression significantly increased DNA damage. (C–E) Impact of differential

RANKL expression on DNA damage markers. (F–G) Differential RANKL expression disrupts microfilament and microtubule organization.

Figure 5A

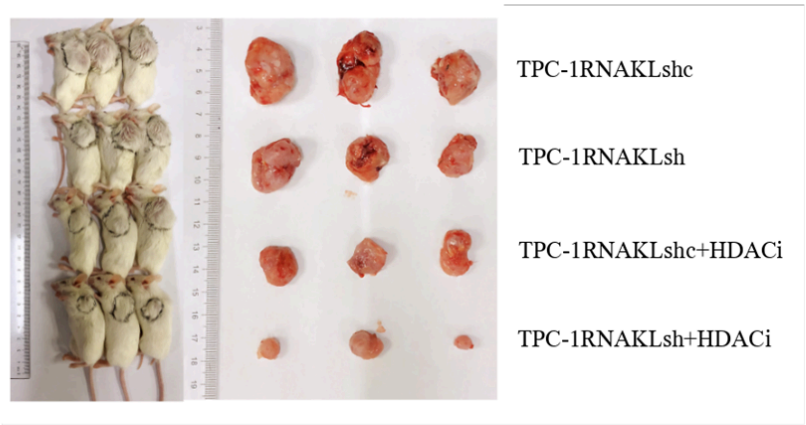


Figure 5B

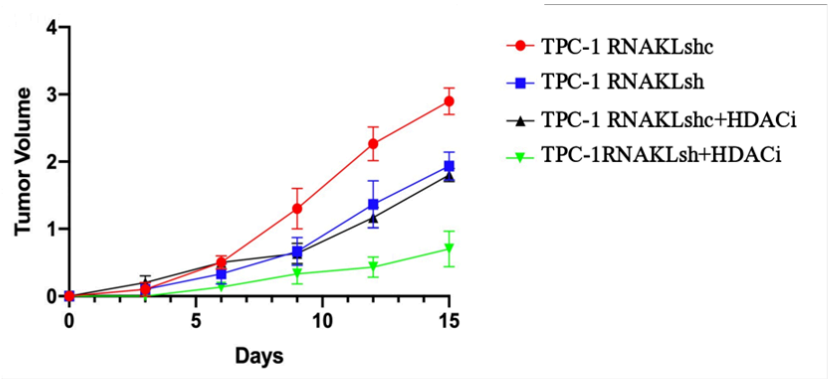


Figure 5C

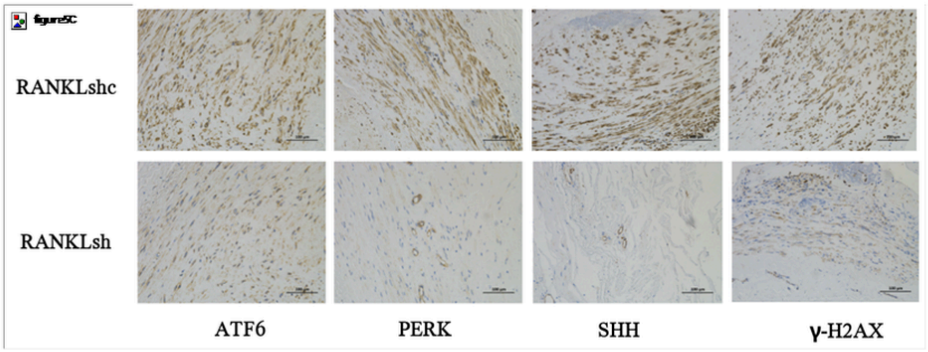


Figure 5

In vivo effects of RANKL knockdown and HDAC inhibition. (A) HDAC inhibition more effectively attenuated tumor growth under conditions of reduced RANKL expression. (B) The HDAC inhibitor

exhibited enhanced tumoricidal efficacy when RANKL expression was downregulated. (C) Immunohistochemistry confirmed that RANKL knockdown modulates DNA damage and ER stress markers.

Supplementary Files

This is a list of supplementary files associated with this preprint. Click to download.

- Supplement.docx
- SupplementaryFigureLegends.docx